

# Planck constraints on the scale dependence of isotropic cosmic birefringence

M. Ballardini,<sup>a,b,c,d</sup> A. Gruppuso,<sup>c,e,a</sup> S. Paradiso,<sup>c,e</sup> S.S. Sirletti<sup>1</sup>,<sup>a,b,f,g</sup> and P. Natoli<sup>a,b,c</sup>

<sup>a</sup>Dipartimento di Fisica e Scienze della Terra, Università degli Studi di Ferrara, via Saragat 1, I-44122 Ferrara, Italy

<sup>b</sup>Istituto Nazionale di Fisica Nucleare, Sezione di Ferrara, via Saragat 1, I-44122 Ferrara, Italy

<sup>c</sup>Istituto Nazionale di Astrofisica - Osservatorio di Astrofisica e Scienza dello Spazio di Bologna, via Gobetti 101, I-40129 Bologna, Italy

<sup>d</sup>Department of Physics & Astronomy, University of the Western Cape, Cape Town 7535, South Africa

<sup>e</sup>Istituto Nazionale di Fisica Nucleare, Sezione di Bologna, viale Berti Pichat 6/2, I-40127 Bologna, Italy

<sup>f</sup>Dipartimento di Fisica, Università di Trento, via Sommarive 14, Trento, 38123, Italy

<sup>g</sup>Department of Physics, Columbia University, New York, NY 10027, USA

E-mail: [mario.ballardini@unife.it](mailto:mario.ballardini@unife.it), [alessandro.gruppuso@inaf.it](mailto:alessandro.gruppuso@inaf.it), [simone.paradiso@inaf.it](mailto:simone.paradiso@inaf.it), [salvatoresamuele.sirletti@unife.it](mailto:salvatoresamuele.sirletti@unife.it), [paolo.natoli@unife.it](mailto:paolo.natoli@unife.it)

**Abstract.** The rotation of the linear polarisation plane of photons during propagation, also known as cosmic birefringence, is a powerful probe of parity-violating extensions of standard electromagnetism. Using *Planck* legacy data, we confirm previous estimates of the isotropic birefringence angle, finding  $\beta \simeq 0.30 \pm 0.05$  [deg] at 68% CL, not including the systematic error from the instrumental polarisation angle. If this is a genuine signal, it could be explained by theories of Chern–Simons-type coupled to electromagnetism, which could lead to a harmonic scale-dependent birefringence signal, if the hypothesis of an ultra-light (pseudo) scalar field does not hold. To investigate these models, we pursue two complementary approaches: first, we fit the birefringence angle estimated at different multipoles,  $\beta_\ell$ , with a power-law model and second, we perform a non-parametric Bayesian reconstruction of it. Both methods yield results consistent with a non-vanishing constant birefringence angle. The first method shows no significant dependence on the harmonic scale (up to  $1.8\sigma$  CL), while the second method demonstrates that a constant model is favored by Bayesian evidence. This conclusion is robust across all four published *Planck* CMB solutions. Finally, we forecast that upcoming CMB observations by Simons Observatory, LiteBIRD and a wishful CMB-Stage 4 experiment could reduce current uncertainties by a factor of approximately 7.

---

<sup>1</sup>Corresponding author.

---

## Contents

<b>1</b>	<b>Introduction</b>	<b>1</b>
<b>2</b>	<b>Planck data and simulations</b>	<b>3</b>
2.1	Angular power spectra	4
<b>3</b>	<b>Testing the harmonic-scale dependence of the isotropic cosmic birefringence</b>	<b>7</b>
3.1	Estimators	7
3.2	Estimates of the $\beta_\ell$	7
3.3	Fitting $\beta_\ell$ with a power-law like functional	11
3.4	Fitting $\beta_\ell$ with a non-parametric Bayesian reconstruction	12
<b>4</b>	<b>Forecasts for future CMB experiments</b>	<b>15</b>
<b>5</b>	<b>Conclusions</b>	<b>15</b>
<b>A</b>	<b>Pivot scale</b>	<b>16</b>
<b>B</b>	<b>Non-parametric Bayesian reconstruction for <math>N \neq 4</math> nodes</b>	<b>16</b>

---

## 1 Introduction

The cosmic birefringence (CB) effect, also known as cosmic polarisation rotation (CPR), is the rotation of the linear polarisation plane of photons in vacuum [1–4]. Parity-violating extensions of standard electromagnetism can produce this effect; the most notable example is Chern-Simons (ChS) theory [1]. Note that this rotation is expected to be zero in the standard Maxwellian scenario, see also Refs. [5, 6]. Since the cosmic microwave background (CMB) radiation is (1) linearly polarised to a few percent level due to Thomson scattering at the last scattering surface, and (2) the most distant known source of linear polarisation in nature, it has become customary to constrain the CB through observations of the CMB polarisation [7].

From an observational point of view, the CB effect induces a mixing between  $E$ - and  $B$ -mode polarisations, which in turn switches on correlations that would not otherwise exist. Specifically, CB affects the observed CMB angular power spectra (APS),  $C_\ell^X$  with  $X = T, E, B$ , as follows [8–10]

$$C_\ell^{TT,\text{obs}} = C_\ell^{TT}, \quad (1.1)$$

$$C_\ell^{TE,\text{obs}} = C_\ell^{TE} \cos(2\beta), \quad (1.2)$$

$$C_\ell^{TB,\text{obs}} = C_\ell^{TE} \sin(2\beta), \quad (1.3)$$

$$C_\ell^{EE,\text{obs}} = C_\ell^{EE} \cos^2(2\beta) + C_\ell^{BB} \sin^2(2\beta), \quad (1.4)$$

$$C_\ell^{BB,\text{obs}} = C_\ell^{BB} \cos^2(2\beta) + C_\ell^{EE} \sin^2(2\beta), \quad (1.5)$$

$$C_\ell^{EB,\text{obs}} = \frac{1}{2} (C_\ell^{EE} - C_\ell^{BB}) \sin(4\beta), \quad (1.6)$$

where  $C_\ell^{X,\text{obs}}$  are the observed CMB APS (i.e. those containing the effect), while on the right-hand side there are the unrotated ones,  $C_\ell^X$ , that would be observed if the birefringence angle  $\beta$  was null. It is important to note that eqs. (1.2) to (1.6) are strictly valid under the assumption that no parity-violation signals are present at the last scattering surface and that the birefringence angle  $\beta$  is constant, see Refs. [11–13] for generalisations. As expected, note also that  $C_\ell^{TT,\text{obs}}$  is not sensitive to the CB effect, as this only affects the CMB polarisation.

The *Planck* collaboration constrained the CB angle to be  $\beta = 0.31 \pm 0.05$  (stat)  $\pm 0.28$  (sys) [deg], where the systematic uncertainty, due to the instrumental polarisation angle (henceforth denoted as  $\alpha$ ) uncertainty, was found to dominate the total error budget [14]. Specifically,  $\alpha$  affects the CMB APS in the same way as described in eqs. (1.2) to (1.6) [15]; therefore, a degeneracy exists between this systematic effect and the cosmological CB effect (see the discussion below). To break this degeneracy, a new technique, now known as the Minami-Komatsu method, was proposed in Refs. [16, 17] and applied to *Planck* data in Ref. [18] and Ref. [19, 20], suggesting a detection of  $\beta$  around 0.3 [deg] with a statistical significance close to  $3\sigma$  confidence level (CL). In particular, WMAP and *Planck* data were analysed jointly in Ref. [21], leading to the exclusion of  $\beta = 0$  at a significance level of  $3.6\sigma$ . See also Ref. [22] for a review of recent constraints on the CB effect. Furthermore, we note that the ACT collaboration has recently suggested an estimate of the birefringence angle,  $\beta_{\text{ACT}} = 0.20 \pm 0.08$  [deg], based on DR6 data [23]. In their analysis, they make use of a detailed optical modelling.<sup>1</sup> See also Ref. [24] for recent estimates of the CB angle from *Planck* Public Data Release 4 data employing a pixel-based estimator.

These estimates are typically interpreted by extending standard electromagnetism.<sup>2</sup> In the context of ChS extensions [2], the photon is coupled to a (pseudo) scalar field  $\chi$ , also called axion or axion-like particle (ALP) depending on the specific potential of the field  $\chi$ , through the following interaction term

$$\mathcal{L}_{\text{int}} = g \chi \tilde{F}_{\mu\nu} F^{\mu\nu}, \quad (1.7)$$

where  $g$  is a coupling constant with dimensions of [energy]<sup>-1</sup>,  $F_{\mu\nu}$  is the electromagnetic tensor and  $\tilde{F}_{\mu\nu}$  is its dual. It can be shown that the eqs. (1.2) to (1.6) are recovered by the ChS theories when  $\chi$  is almost constant in time during the recombination epoch [26]. This occurs when the mass of the field is sufficiently small for a fixed coupling constant  $g$ . This qualitative behaviour appears to be largely independent of the potential considered for  $\chi$  [27]. On the contrary, if the mass is larger,  $\chi$  exhibits a time-evolution (characterized by a decay followed by damped oscillations) that modifies these relations. As a consequence, in ChS extensions of standard electromagnetism, the degeneracy between  $\alpha$  and  $\beta$  is exact when the mass of the ALP is ultra-light, otherwise such a degeneracy is broken, see also Refs. [28–30]. In Ref. [31] the dependence on the mass of the ALP is studied through a related effect, the anisotropic birefringence.

From an observational perspective, the degeneracy is maximised when  $\beta$  is independent of the harmonic scale. Previous analyses of *Planck* measurements [32] suggest that this scenario is currently favoured by the data. Similar conclusions are obtained in [33], where constraints on the ALPs parameters are derived from the full shape of the *Planck* *EB* spectrum. In this work, we propose a new test to assess whether  $\beta$  is indeed independent of the

<sup>1</sup>While this ACT constraint is noteworthy, it is obtained without a dedicated component separation step, and also does not account for pointing uncertainty, which is of the order of 0.03 [deg], see again Ref. [23].

<sup>2</sup>See also Ref. [25] for an interpretation based on non-trivial spatial topology, which leaves standard electromagnetism unchanged.

harmonic scale. We use *Planck* Public Data Release 3 (henceforth PR3) [34] to estimate the birefringence angles at different harmonic scales, hereafter denoted as  $\beta_\ell$ , and we test their consistency across the entire harmonic range.<sup>3</sup> This is performed in two different ways, as detailed below:

1. In the first approach, we fit the estimated angles at different angular scales using a two-parameter power-law model,  $(\beta_0, n)$ , defined as  $\beta_\ell = \beta_0 (\ell/\ell_0)^n$ , where  $\ell_0$  is a suitable harmonic pivot scale.<sup>4</sup> In this approach, the power  $n$  is the key parameter, as it quantifies the consistency of a constant birefringence angle across the entire harmonic range under consideration.
2. In the second approach, we fit  $\beta_\ell$  using a non-parametric Bayesian reconstruction for a given number of moving knots [35–37]. In this case, the best-fit curve is statistically evaluated against constant behavior in  $\ell$ .

We anticipate that the first method indicates that the CB angle is independent of the harmonic scale up to  $1.8\sigma$  CL. A consistent result is obtained with the second approach, i.e. the non-parametric method, where a constant birefringence angle is preferred in terms of Bayesian evidence against more flexible models that require a larger number of parameters.

The paper is organised as follows. In section 2, we describe the *Planck* data and the corresponding simulations used in our analyses. In particular, we compute the CMB spectra for both simulations and data, and assess the statistical significance of the deviation of the *EB* spectrum from zero. In section 3, we test the harmonic-scale dependence of the CB angle. Specifically, in section 3.2, we estimate the birefringence angles in different harmonic ranges,  $\beta_\ell$ , and characterise their covariance using simulations. These  $\beta_\ell$  values are then fitted with a power-law model in section 3.3, and interpolated using a non-parametric approach in section 3.4. In section 4 we provide forecasts for future CMB experiments. Finally, in section 5, we present our conclusions, along with a statistical assessment of the results.

## 2 Planck data and simulations

In this work, we employ *Planck* PR3 data and simulations [34]. Specifically, we make use of the official *Planck* CMB maps obtained through four component-separation (CS) methods: *Commander* [38, 39], *NILC* [40], *SEVEM* [41], and *SMICA* [42, 43]. These methods process multi-frequency observations to extract the CMB signal, cleaned from foreground emissions [44, 45]. In order to statistically characterize the data, we exploit the official *Planck* PR3 simulations. For each CS method, the simulation set consists of 1000 CMB Monte Carlo simulations generated using the *Planck*  $\Lambda$ CDM best-fit model (also referred to as the fiducial model) [45] including a beam modeling,<sup>5</sup> along with 300 noise simulations for the first half-mission (HM1) and 300 for the second half-mission (HM2). The *Planck* PR3 simulations include residuals from several systematic effects, such as beam leakage, analog-to-digital converter (ADC) non-linearities, thermal fluctuations, and others [48, 49]. All product used here are publicly available on the ESA *Planck* Legacy Archive<sup>6</sup> and are used at  $N_{\text{side}} = 2048$ , where

<sup>3</sup>Note that the goal of this paper is not to address the degeneracy between  $\beta$  and  $\alpha$  directly. However, the proposed test may help to distinguish between the two.

<sup>4</sup>As will become clear in the following sections, the power-law functional is actually employed in a slightly different form, where the harmonic dependence is expressed in terms of band powers.

<sup>5</sup>In polarization this is equivalent to an effective Gaussian beam of 5 arcmin, see Refs. [46, 47].

<sup>6</sup><http://pla.esac.esa.int/pla>

$N_{\text{side}}$  is a parameter of the Hierarchical Equal Area isoLatitude Pixelization of a sphere (HEALPix) pixelisation scheme [50],<sup>7</sup> which is related to the number of pixels,  $N_{\text{pix}}$ , through  $N_{\text{pix}} = 12N_{\text{side}}^2$ .

## 2.1 Angular power spectra

For each CS method, we build two data splits by co-adding the 300 HM1 and the 300 HM2 noise simulations with the first 300 CMB simulations. These splits are then used to estimate the CMB APS in cross-mode, which is known to provide auto-spectra that are less sensitive to noise details and residual systematic effects [45]. The APS are computed using the NaMaster Python package [51],<sup>8</sup> which implements the so-called pseudo- $C_\ell$  approach [52, 53]. This computation takes into account the *Planck* PR3 common masks for intensity and polarisation, as well as the masks covering unobserved pixels in HM1 and HM2, see fig. 1. No mask apodization or purification [54–56] is applied. See also Ref. [46] though employing different sky coverage and band powers. Figures 2 and 3 display  $\mathcal{D}_\ell^{EB} \equiv \ell(\ell + 1)C_\ell^{EB}/2\pi$

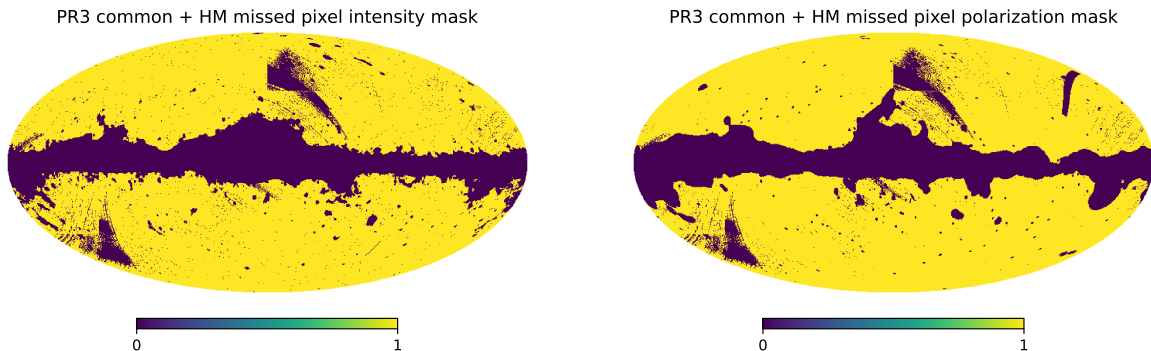


**Figure 1:** Masks used in this work. Both the intensity (left panel) and polarization (right panel) masks have an effective sky fraction of  $f_{\text{sky}} \simeq 75\%$ .

and  $\mathcal{D}_\ell^{(EE-BB)/2} \equiv \ell(\ell + 1) [(C_\ell^{EE} - C_\ell^{BB})/2] / 2\pi$ , respectively. This specific APS choice is motivated by the analysis pipeline described in section 3.2. Each of these figures contains four panels, one for each CS method, presenting the binned APS with bandpowers of  $\Delta\ell = 20$  up to a maximum multipole  $\ell_{\text{max}} \simeq 1550$ . In each panel, we illustrate the data APS with error bars (estimated from the simulations) in black, the  $\Lambda$ CDM fiducial spectrum in dotted gray, and the mean with one  $\sigma$  dispersion from the simulations in orange. The lower part of each panel shows how well the simulations are compatible with the expected fiducial APS, denoted by  $\mathcal{D}_\ell^{X,\text{fid}}$ , where  $X = \{EB, (EE - BB)/2\}$ . To achieve this, we plot *standardised* APS, defined as:

$$\Delta\mathcal{D}_\ell^X \cdot (\bar{C}^X)_{\ell\ell'}^{-1/2},$$

where,  $\Delta\mathcal{D}_\ell^X = \langle \mathcal{D}_\ell^X - \mathcal{D}_\ell^{X,\text{fid}} \rangle$  represents the mean difference from the fiducial spectrum. The term  $(\bar{C}^X)_{\ell\ell'}^{-1/2}$  is the Cholesky decomposition of the inverse of the mean covariance,  $\bar{C}_{\ell\ell'}^X$ . The latter is calculated as  $C_{\ell\ell'}^X/300$ , where  $C_{\ell\ell'}^X$  is the covariance of  $X$ . These quantities are assumed to be approximately normal distributed with zero mean and unitary standard deviation at each harmonic bandpower, and therefore expected to lie mostly within  $\pm 3\sigma$ . The

<sup>7</sup><https://sourceforge.net/projects/healpix/>

<sup>8</sup><https://namaster.readthedocs.io>

covariances  $C_{\ell\ell'}^X$  are computed using an analytical approach provided by the `NaMaster` code, which includes the fluctuations of signal and noise, as well as the mode coupling induced by the sky masking, see again Ref. [51].

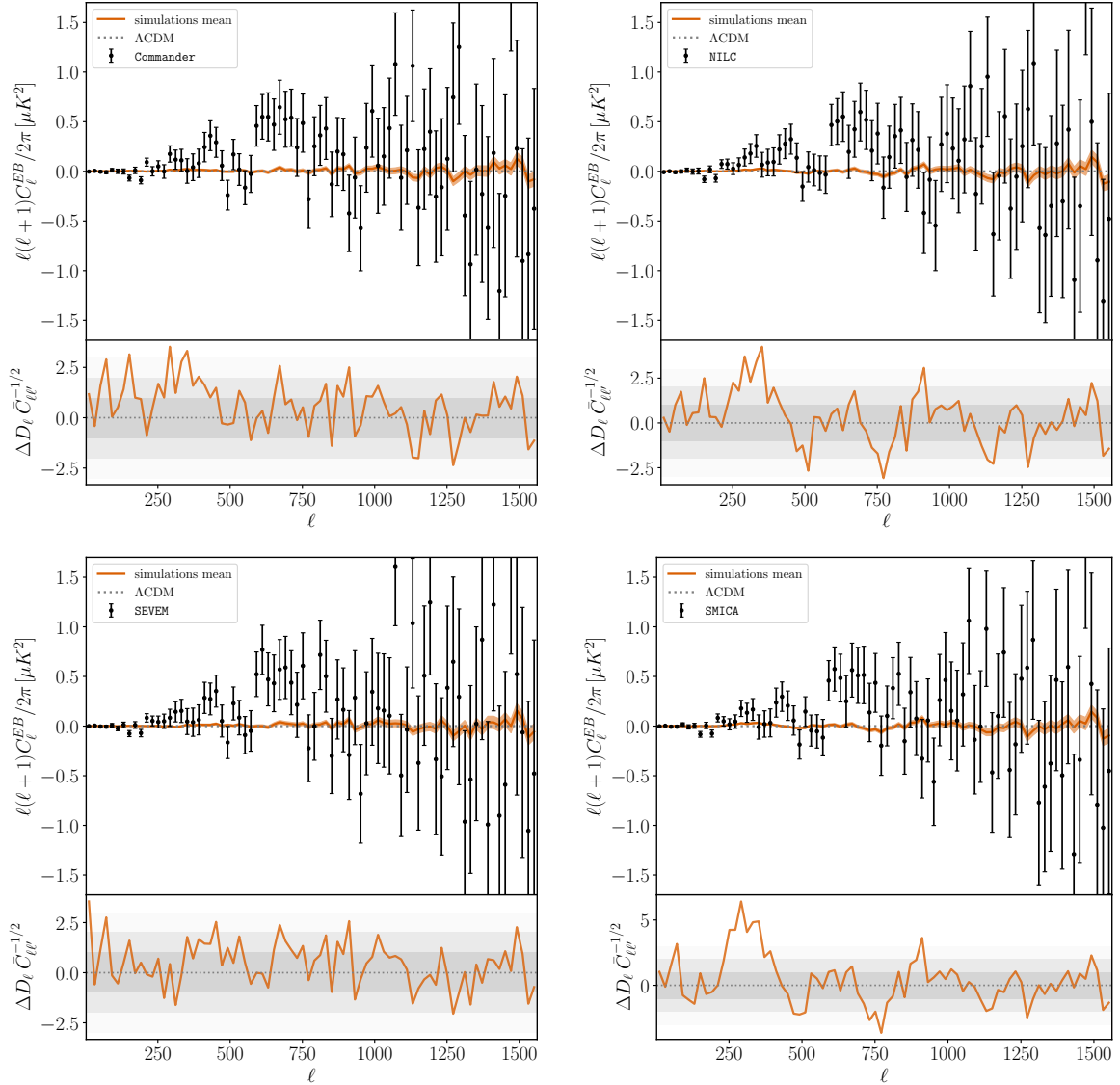


**Figure 2:**  $\mathcal{D}_\ell^{EB} \equiv \ell(\ell + 1)C_\ell^{EB}/2\pi [\mu\text{K}^2]$  versus  $\ell$  from *Planck* PR3 data binned with  $\Delta\ell = 20$ . The panels are organised by CS method: upper left panel for `Commander`, upper right for `NILC`, lower left for `SEVEM`, and lower right for `SMICA`. In each panel, the upper part shows the APS with error bars (black), the  $\Lambda\text{CDM}$  fiducial spectrum (dotted gray), and the mean with one  $\sigma$  dispersion of the mean from the simulations (orange). The lower part shows the fluctuation of the mean of the simulations relative to the fiducial spectrum in units of the standard deviation of the mean.

The lower panels of figs. 2 and 3 show that the simulation average deviates by less than  $3.5\sigma$  from the fiducial for all the considered CS methods. This indicates that the residuals present in the official *Planck* simulations do not exhibit any significant systematic behaviour.

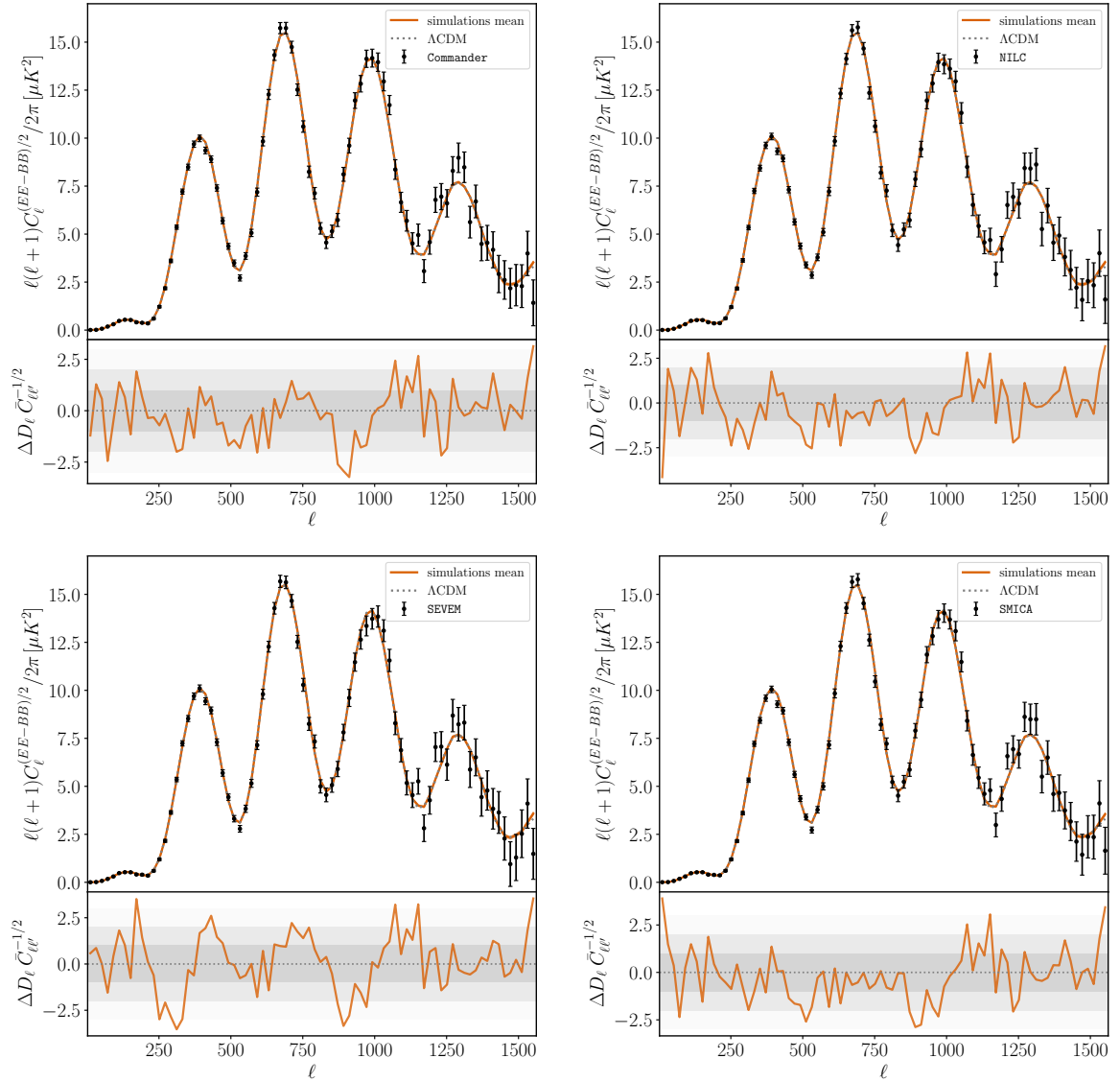


**Figure 3:**  $\mathcal{D}_\ell^{(EE-BB)/2} \equiv \ell(\ell+1)[(C_\ell^{EE} - C_\ell^{BB})/2]/2\pi$   $[\mu K^2]$  versus  $\ell$  from *Planck* PR3 data binned with  $\Delta\ell = 20$ . The panels are organized by CS method: upper left panel for **Commander**, upper right for **NILC**, lower left for **SEVEM**, and lower right for **SMICA**. In each panel, the upper part shows the APS with error bars (black), the  $\Lambda$ CDM fiducial spectrum (dotted grey), and the mean with one  $\sigma$  dispersion of the mean from the simulations (orange). The lower part shows the fluctuation of the mean of the simulations relative to the fiducial spectrum in units of the standard deviation of the mean.

The sole outstanding exception is observed for **SMICA** in  $\mathcal{D}_\ell^{EB}$  around  $\ell \simeq 300$ , where a fluctuation of  $\sim 5\sigma$  is found. However, such a deviation corresponds to only around 30% of the APS statistical uncertainty at those angular scales. Therefore, we do not expect this excess to significantly impact our results. Moreover, to reinforce this point, the corresponding **SMICA** estimates are well consistent with those derived from the other CS methods, even around  $\ell \simeq 300$  where the simulations of the other CS methods do not exhibit any significant

deviation from the expected statistical fluctuations.

In summary, we find excellent consistency of the APS estimates for both  $\mathcal{D}_\ell^{EB}$  and  $\mathcal{D}_\ell^{(EE-BB)/2}$  at better than  $2\sigma$  level across all the CS methods. Moreover, a harmonic  $\chi^2$ -analysis<sup>9</sup> reveals an excess for  $\mathcal{D}_\ell^{EB}$ , while it exhibits very good agreement for  $\mathcal{D}_\ell^{(EE-BB)/2}$  across all CS methods. Specifically, the value of the  $\chi_{\text{data}}^2$  for  $\mathcal{D}_\ell^{EB}$  ranges from 96 to 115 (depending on the CS method), whereas the expected  $\chi^2$  value is 73, corresponding to the harmonic range [42, 1501]. These values indicate a compatibility of the  $EB$  spectrum with zero (expressed as the probability to exceed) ranging from 0.2% for **Commander**, 0.3% for **NILC**, 0.1% for **SEVEM**, and 0.7% for **SMICA**.

### 3 Testing the harmonic-scale dependence of the isotropic cosmic birefringence

In this section, we first introduce the CB estimator from the CMB APS and the estimator we use to evaluate the CB at different angular scales. We then present our findings based on *Planck* data.

#### 3.1 Estimators

Starting from eqs. (1.1) and (1.6), it is possible to construct two harmonic-based estimators for  $\beta$ , known as  $D$ -estimators [14, 57, 58]

$$D_\ell^{TB,\text{obs}}(\hat{\beta}) \equiv C_\ell^{TB,\text{obs}} \cos(2\hat{\beta}) - C_\ell^{TE,\text{obs}} \sin(2\hat{\beta}), \quad (3.1)$$

$$D_\ell^{EB,\text{obs}}(\hat{\beta}) \equiv C_\ell^{EB,\text{obs}} \cos(4\hat{\beta}) - \frac{1}{2} \left( C_\ell^{EE,\text{obs}} - C_\ell^{BB,\text{obs}} \right) \sin(4\hat{\beta}), \quad (3.2)$$

where  $\hat{\beta}$  is the estimate of the CB angle  $\beta$ . It can be shown, see e.g. [58], that

$$D_\ell^{Y,\text{obs}}(\hat{\beta} = \beta) = 0, \quad (3.3)$$

for  $Y = TB$  or  $EB$ . Equation (3.3) suggests that  $\beta$  can be found identifying the zeros of the  $D$ -estimators. In the following, we base our analysis on  $D_\ell^{EB,\text{obs}}(\hat{\beta})$ , which is known to have greater constraining power than  $D_\ell^{TB,\text{obs}}(\hat{\beta})$  for *Planck* [14].<sup>10</sup>

#### 3.2 Estimates of the $\beta_\ell$

The first part of our analysis consists of recovering previous results already present in the literature. We estimate the CB angle by minimising the following  $\chi^2(\hat{\beta})$

$$\chi^2(\hat{\beta}) = \sum_{b,b'} D_b^{EB,\text{obs}}(\hat{\beta}) (C^{EB})_{bb'}^{-1} D_{b'}^{EB,\text{obs}}(\hat{\beta}), \quad (3.4)$$

considering the whole range of multipoles, where  $b, b' = 1, \dots, 73$ , corresponding to the harmonic range [42, 1501], which is equally spaced with  $\Delta\ell = 20$ , and with  $C_{bb'}^{EB}$  being the analytical covariance matrix for  $EB$  computed through **NaMaster**, see section 2.1. As also

<sup>9</sup> $\chi^2 = \sum_{\ell,\ell'} \mathcal{D}_\ell^X C_{\ell\ell'}^X{}^{-1} \mathcal{D}_{\ell'}^X$ , with  $X = \{EB, (EE - BB)/2\}$ .

<sup>10</sup>This statement is strictly true when the full available harmonic range is considered. It is possible that for very specific subranges the two estimators have closer statistical efficiency. We plan to return to this point in future investigations.

done in previous analyses, see e.g. [14], we exclude the lowest multipoles to mitigate possible residual of systematic effects (including those of astrophysical origin). For each CS method, we compute  $\beta$  for each simulation and for the corresponding *Planck* CMB solution. These values were used to construct fig. 4, where the histograms represent the expected distribution from simulations for each CS method, and the vertical bars indicate the observed CB angle. In each panel, we also display a Gaussian distribution, whose mean and standard deviation are derived from the corresponding histogram. This normal distribution is used to compute the significance of the observed value, which is also reported above the arrow connecting the mean of the histograms to the estimated angle. The probabilities associated with the observations range from  $5\sigma$  of the SMICA solution to  $6.2\sigma$  of NILC, whereas we find  $5.4\sigma$  and  $5.3\sigma$  for Commander and SEVEM, respectively. The estimated means and standard deviations of the  $\beta$ s are reported in table 1, along with the residual CB angle  $\beta_{\text{res}} = \langle \beta_i \rangle_{i \in \text{sims}}$  computed on the simulations. Note that the latter corresponds to a fraction of the statistical uncertainty associated with the  $\beta$  and is therefore not responsible for the overall measured CB effect. However, it can be interpreted as a source of systematic uncertainty.

Method	$\beta$ [deg]	$\beta_{\text{res}}$ [deg]
PR3 Commander	$0.30 \pm 0.05$	0.02
PR3 NILC	$0.32 \pm 0.05$	0.01
PR3 SEVEM	$0.31 \pm 0.06$	0.01
PR3 SMICA	$0.27 \pm 0.05$	0.02

**Table 1:** Values of  $\beta$  obtained over the harmonic range [42,1501] for the four CS methods considered in this work. In the third column, we report the mean value of the CB angle estimated from the simulations,  $\beta_{\text{res}}$ .

We then evaluate the CB angle,  $\beta_B$ , over four harmonic bins,  $b$ , by minimizing the following  $\chi_B^2(\hat{\beta}_B)$

$$\chi_B^2(\hat{\beta}_B) = \sum_{b,b'} D_b^{EB,\text{obs}}(\hat{\beta}_B) (C^{EB})_{bb'}^{-1} D_{b'}^{EB,\text{obs}}(\hat{\beta}_B), \quad (3.5)$$

where  $B$  labels four aggregated consecutive bins  $b$  in order to cover the multipole range [42,1481].<sup>11</sup> In this way  $B \in [1, 18]$  is mapping  $b \in [1, 72]$ . For each CS method and for each of the 300 corresponding simulations, we have computed the values  $\beta_B$  that correspond to the minimum of eq. (3.5). We have then estimated their covariance from simulations as

$$C_{BB'}^\beta = \langle (\beta_B - \langle \beta_B \rangle) (\beta_{B'} - \langle \beta_{B'} \rangle) \rangle, \quad (3.6)$$

where  $\langle \beta_B \rangle$  is the mean over the simulations for each bin  $B$ . Using the same procedure, we estimate  $\beta_B$  from *Planck* data. Results are displayed in fig. 5. For each panel in the figure, we illustrate the compatibility of  $\langle \beta_B \rangle$  with the null hypothesis in the lower tiles. This is shown through the quantity  $\langle \beta_B \rangle \left[ H \cdot (C_{BB'}^\beta)^{-1} \right]^{1/2}$  (solid orange lines), which is expected to lie mostly within  $\pm 3\sigma$  for each bin  $B$ . The inverse covariance matrix is corrected using

<sup>11</sup>We excluded the last bin,  $b = 73$ , to make the total number of bins divisible by four. Additionally, we have found that the estimate of  $\beta$  on the aggregated bins corresponding to the multipole range  $\ell \in [2, 41]$ , carries an uncertainty approximately 10 times larger than that obtained from the same analysis conducted on the aggregated harmonic bins in  $\ell \in [42, 1481]$ .

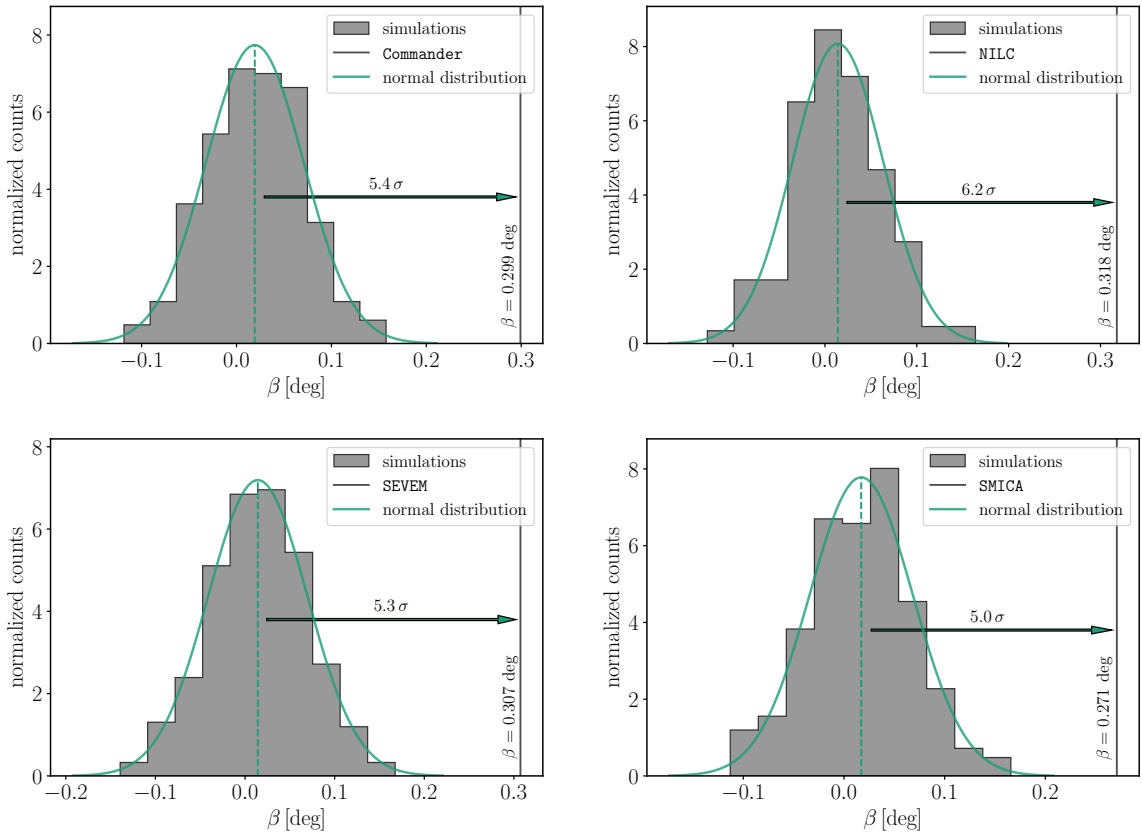


**Figure 4:** Estimated  $\beta$  for all the CS methods: upper left panel for **Commander**, upper right for **NILC**, lower left for **SEVEM** and lower right for **SMICA**. In each panel, the histogram (in gray), built with simulations, represents the expected distribution for  $\beta$ , the vertical bar (in black) stands for the observed value. The curve (in green) is a Gaussian distribution, whose mean and standard deviation are derived from the corresponding histogram. This normal distribution is used to calculate the significance of the observed value (also reported above the arrow connecting the mean of the histograms to the estimated angle).

the Hartlap factor  $H$  to account for the limited number of effective degrees of freedom in the simulation-based covariance estimate [59]. Note also that, as before, with the power of  $1/2$  applied to a given matrix, we mean the Cholesky decomposition of the same matrix. We also perform the same calculation using only the diagonal elements of  $C_{BB'}^\beta$ , this time without applying the Hartlap correction (dashed lines). As can be seen in fig. 5, the off-diagonal terms contribute negligibly to the total uncertainty. This test reveals only partial compatibility of the *Planck* simulations processed with **Commander**, **NILC**, and **SMICA**, as evidenced by excess power around  $\ell \approx 300$  for all three CS methods, and additionally around  $\ell \approx 500$  and  $700$  for **NILC** and **SMICA**. To address this, we applied a debiasing procedure, subtracting the constant residual value  $\beta_{\text{res}}$  – see table 1 – from each  $\beta_B$ , separately for each CS method. We then re-evaluated the standardised quantities and present the results – now debiased – in the same lower tiles of fig. 5, using indigo lines to indicate the corrected curves. This procedure restores full compatibility with the null hypothesis for **Commander**, whereas it only mildly mitigates the residual excess for **NILC** and **SMICA**. **SEVEM** exhibits full compatibility regardless of the

debiasing procedure. We will comment on the impact of the residual excess in the analysis section. Nevertheless, we note that all estimates obtained from the different CS methods are

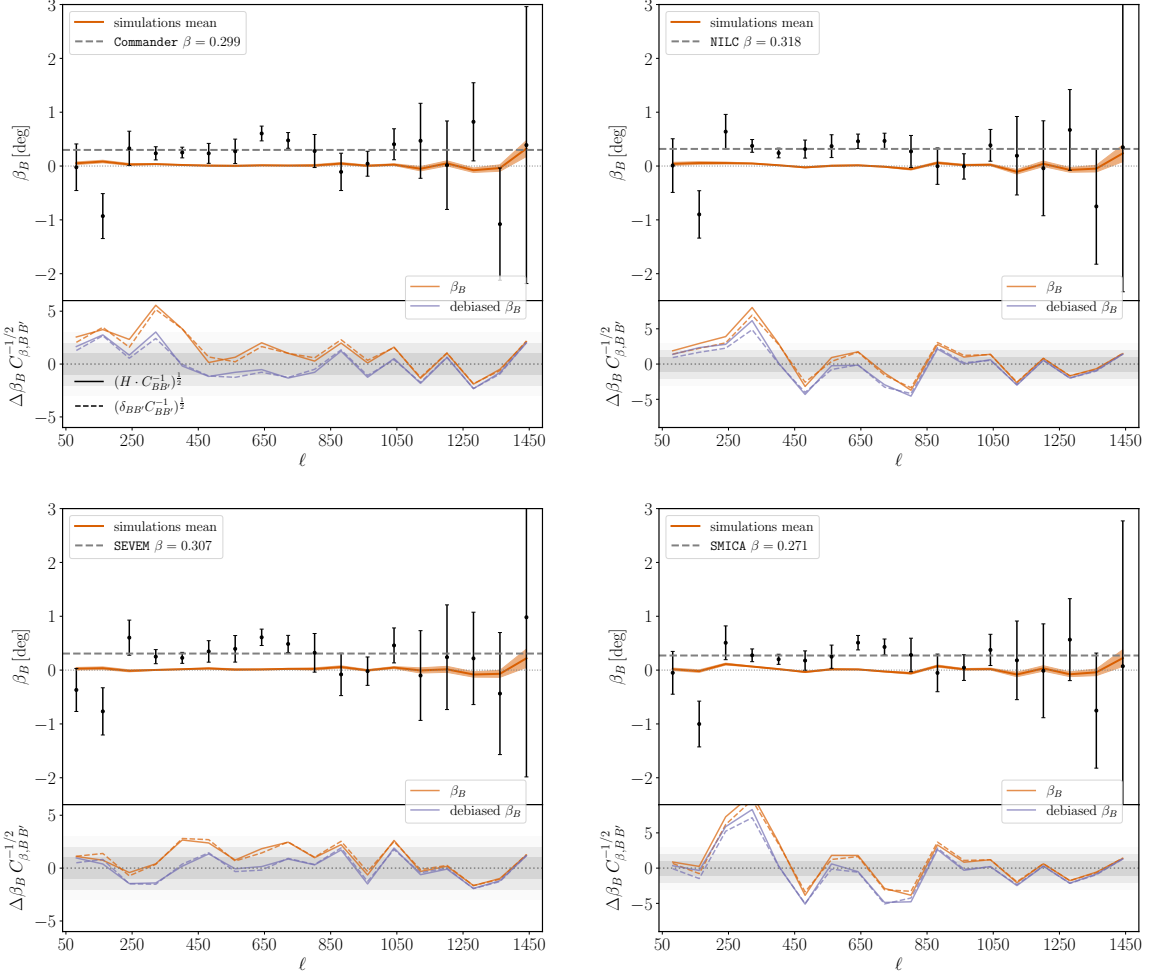


**Figure 5:** Estimated  $\beta_B$  for all the CS methods: upper left panel for Commander, upper right for NILC, lower left for SEVEM, and lower right for SMICA. In each panel we report the values of  $\beta_B$  from data (black) with errorbars computed from the numerical covariance  $C_{BB'}^\beta \delta_{BB'}$  and the mean value,  $\langle\beta_B\rangle$ , with its  $1\sigma$  area from the corresponding simulations (orange); grey dashed lines indicate the value of  $\beta$  computed on the whole multipole range. In the lower tile we show the fluctuation of the simulations' mean with respect to the null hypothesis before removing the constant value of  $\beta_{\text{res}}$  at each multipole (orange) and after (indigo), and considering the full dense covariance matrix corrected by the Hartlap factor (solid) or only its diagonal (dashed).

in very good agreement, with relative fluctuations typically around  $1\sigma$  level.<sup>12</sup>

<sup>12</sup>This is not true in the excluded multipole range [2,41].

Par.	Data	Commander	NILC	SEVM	SMICA
$\beta_0$ [deg]	$\beta_B$	$0.28 \pm 0.05$	$0.31 \pm 0.05$	$0.30 \pm 0.06$	$0.26 \pm 0.05$
	$\beta_{\text{res}}$	$0.019 \pm 0.003$	$0.013 \pm 0.003$	$0.013 \pm 0.003$	$0.017 \pm 0.003$
	$\beta_B - \beta_{\text{res}}$	$0.26 \pm 0.05$	$0.29 \pm 0.05$	$0.29 \pm 0.06$	$0.25 \pm 0.05$
$n$	$\beta_B$	$0.60^{+0.34}_{-0.31}$	$0.29^{+0.31}_{-0.29}$	$0.57^{+0.33}_{-0.31}$	$0.52^{+0.36}_{-0.34}$
	$\beta_{\text{res}}$	$0.00^{+0.35}_{-0.31}$	$0.00^{+0.45}_{-0.41}$	$0.00^{+0.49}_{-0.41}$	$0.00^{+0.38}_{-0.33}$
	$\beta_B - \beta_{\text{res}}$	$0.62^{+0.36}_{-0.33}$	$0.30 \pm 0.31$	$0.59^{+0.34}_{-0.32}$	$0.54^{+0.38}_{-0.35}$

**Table 2:** Best-fit values and  $1\sigma$  errors for  $(\beta_0, n)$  from different CS methods, and different inputs: data  $\beta_B$ , bias  $\beta_{\text{res}}$ , and debiased data  $\beta_B - \beta_{\text{res}}$ .

### 3.3 Fitting $\beta_\ell$ with a power-law like functional

In this section, we estimate the birefringence angles  $\beta_B$  across angular scales using a two-parameter power-law model defined as

$$\beta(B) = \beta_0 \left( \frac{\ell_B}{\ell_{B_0}} \right)^n, \quad (3.7)$$

where  $\beta_0$  is the amplitude,  $n$  is the power (or slope) that characterizes the harmonic scale dependence at a reference pivot scale  $\ell_{B_0}$ . The power index  $n$  is the key parameter in this analysis, as it quantifies deviations from a constant birefringence angle across multipoles. Since the power-law form in eq. (3.7) is sensitive to the choice of pivot, we fix  $B_0$  to the bin which minimises the correlation between  $\beta_0$  and  $n$ , while also providing the smallest systematic uncertainty coming from  $\beta_{\text{res}}$ . This corresponds to the sixth bin, with  $\ell_{B_0=6} \in [442, 522]$ , which is consistent across all four CS methods, see appendix A for details. We developed the following pipeline in order to test the power-law model in eq. (3.7):

1. we construct a two-dimensional grid  $(\beta_0, n)$  centered at  $(0, 0)$ . It consists of  $1000 \times 1000$  points, spanning the ranges  $\beta_0 \in [-1, 1]$  deg and  $n \in [-1.5, 2.5]$ ;
2. we then evaluate the value of a 2-dimensional  $\chi^2$  at each value of the grid  $(\beta_0, n)$ , assuming the theoretical power law in eq. (3.7);
3. we minimize the 2-dimensional  $\chi^2$  to find the best-fit values  $(\beta_0, n)$ .

The  $\chi^2(\beta_0, n)$  has the following expression

$$\chi^2(\beta_0, n) = \sum_{B, B'}^{18} [\beta(B) - \beta_B] \left( C^\beta \right)_{BB'}^{-1} [\beta(B') - \beta_{B'}], \quad (3.8)$$

where  $\chi^2(\beta_0, n)$  quantifies the goodness of fit for each point on the grid. This procedure has been applied to  $\beta_B$  as obtained from each CS methods, to  $\beta_{\text{res}}$  to propagate the systematic effect to the parameters, and to the *debiased* dataset,  $\beta_B - \beta_{\text{res}}$ .

We display the marginal distributions for  $(\beta_0, n)$  in fig. 6, and report in table 2 the constraints on  $\beta_0$  and  $n$ . The constraints on the input  $\beta_{\text{res}}$  represent a systematic effect that contributes only to  $\beta_0$  at the level of  $\sim 40\%$  of the statistical uncertainty. In particular, the

systematic uncertainty on  $n$  peaks at zero and therefore possible residuals from the *Planck* analysis pipeline do not represent a significant limitation to our analysis. Our estimates of  $n$  are compatible with zero within the total error budget at the level of  $1.8\sigma$  for **Commander**,  $1.0\sigma$  for **NILC**,  $1.7\sigma$  for **SEVEM**, and  $1.5\sigma$  for **SMICA**. However, when we build templates for **NILC** and **SMICA** in order to cope with the excess found at  $\ell \approx 300, 500$  and  $700$ , see again fig. 5, we obtain  $\beta_0 = 0.30 \pm 0.05$  [deg] and  $n = 0.40 \pm 0.33$  for **NILC** and  $\beta_0 = 0.25 \pm 0.05$  [deg] and  $n = 0.68 \pm 0.36$  for **SMICA**. This means that the shift in the power index,  $n$ , is  $-0.11$  for **NILC** and  $-0.16$  for **SMICA**, corresponding to fractions of a standard deviation of  $0.36\sigma$  and  $0.51\sigma$ , respectively. This suggests a non-negligible interplay between foreground contamination and systematic residuals; accounting for this yields updated estimates of the power index that are compatible among the different CS methodologies within one  $\sigma$ . The templates are built using the means of  $\beta_B$  computed from simulations (without debiasing, see the orange lines in fig. 5), selecting only those fluctuations above  $3.5\sigma$ . We then estimate  $\beta_0$  and  $n$  on the dataset after subtracting the template.

### 3.4 Fitting $\beta_\ell$ with a non-parametric Bayesian reconstruction

To model the data in a way that avoids theoretical biases, we adopt a model-independent reconstruction approach based on a flexible representation using moving nodes or knots. This method provides a versatile framework that allows the data to guide the shape of the reconstructed function without relying on a specific parametric model, as we did in the previous section.

Reconstruction is performed by placing a set of nodes along the domain of the data. The amplitudes and positions of these nodes are treated as free parameters to be inferred from the data performing a Bayesian analysis. The function between the nodes is interpolated using a linear spline. This approach, commonly known as **FlexKnot** model [60], allows the reconstruction to flexibly adapt to the underlying data structure. To ensure the robustness and generality of the reconstruction, the two endpoints of the domain are fixed at  $\ell_{\min} = 42$  and  $\ell_{\max} = 1481$ , while the intermediate nodes are allowed to vary in a sorted manner, i.e. ordered such that  $\ell_i < \ell_{i+1}$  for any node  $i$  to avoid encountering in a non-physical form. The number of nodes is increased incrementally, starting with one node ( $N = 1$ ), corresponding to a constant amplitude, and progressively adding more nodes ( $N = 2, 3, 4, \dots$ ). This iterative approach allows us to assess the trade-off between model complexity and quality of fit.

Inference is performed using the nested sampling algorithm implemented in **PyPolyChord** [35, 36]<sup>13</sup> with 800 live points. We consider the isotropic birefringence angle estimates as obtained in section 3.2 for all the four CS methods. The log-likelihood function, i.e. eq. (3.8), incorporates the observed data and their uncertainties, while the priors are chosen to reflect reasonable physical constraints on the node amplitudes and positions. Amplitudes have been sampled with a uniform prior between  $[-20^\circ, 20^\circ]$  and positions have been sampled with a uniform prior between  $[\ell_{\min}, \ell_{\max}]$  applying a *forced identifiability prior* transformation [36, 61]. For each configuration of the number of nodes, the posterior distributions of the parameters are obtained and the model evidence is computed. The Bayesian evidence provides a quantitative metric for comparing reconstructions with different numbers of nodes, allowing us to identify the optimal balance between model simplicity and explanatory power. The posterior distributions of the reconstructed functions are visualized using the **fgivenx** package [62],<sup>14</sup> which provides a clear representation of the uncertainty in the reconstruction.

<sup>13</sup><https://github.com/PolyChord/PolyChordLite>

<sup>14</sup><https://github.com/handley-lab/fgivenx>

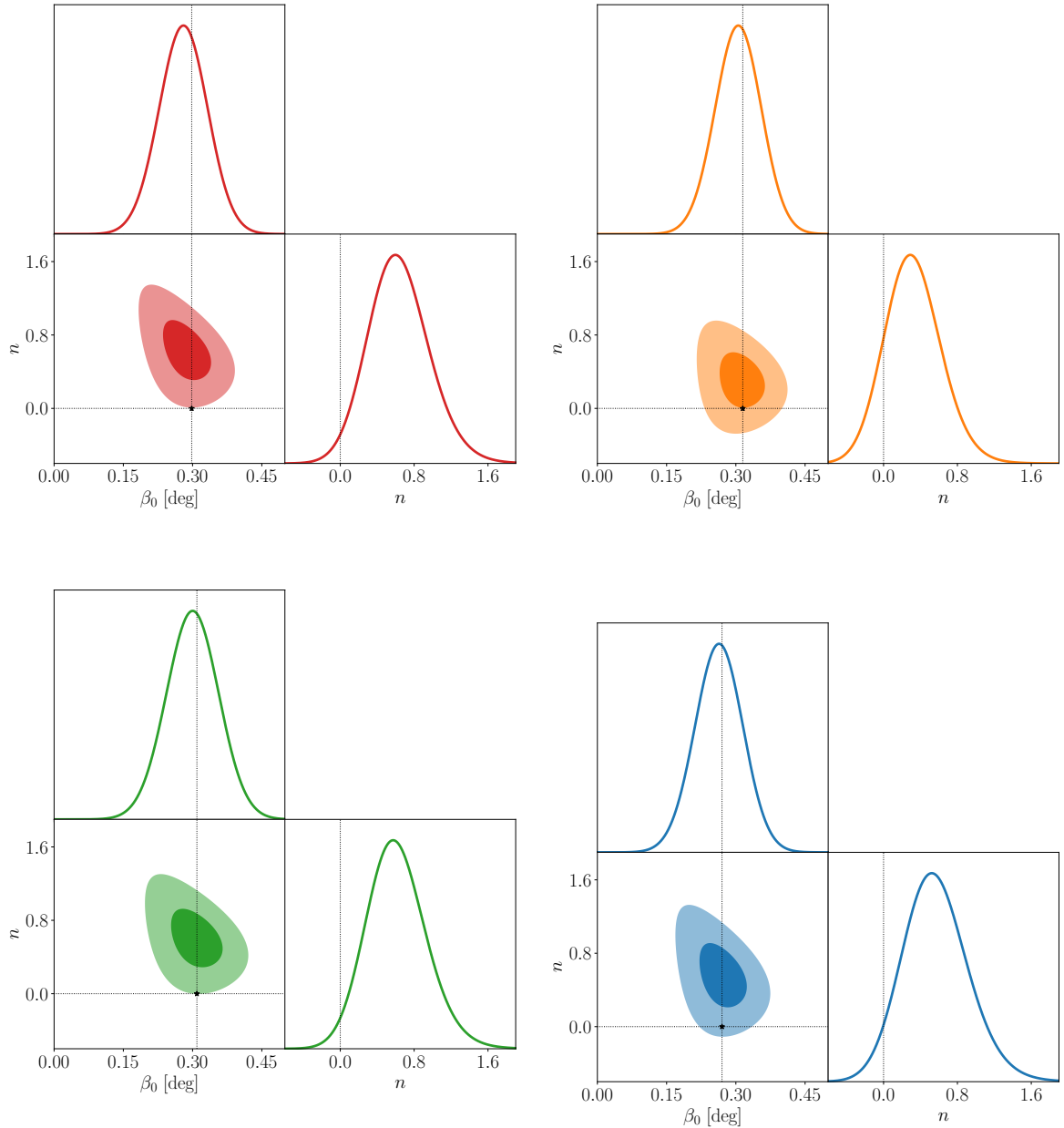


**Figure 6:** Triangular plots illustrating the power-law constraints for all four CS methods using  $D^{EB}$  estimator: upper left panel for **Commander**, upper right for **NILC**, lower left for **SEVEM**, and lower right for **SMICA**. The  $\star$  represent  $(\beta, 0)$  with  $\beta$  given in table 1.

Figure 7 shows the reconstructed function obtained with the four CS methods, assuming  $N = 4$ . The shaded regions represent the credible intervals derived from the posterior samples. We compare the reconstructed  $\beta_\ell$  spectra for  $N = 4$  with the results obtained in the single-node case, i.e.  $N = 1$ , displayed as grey shadow region in fig. 7, and reported in table 3. While all four CS methods yield consistent results, broadly agreeing with a constant CB angle, small deviations at 68% CL appear at large angular scales ( $\ell \lesssim 350$ ) for **Commander**, **SEVEM**, and **SMICA**, where the results are more compatible with a vanishing angle.

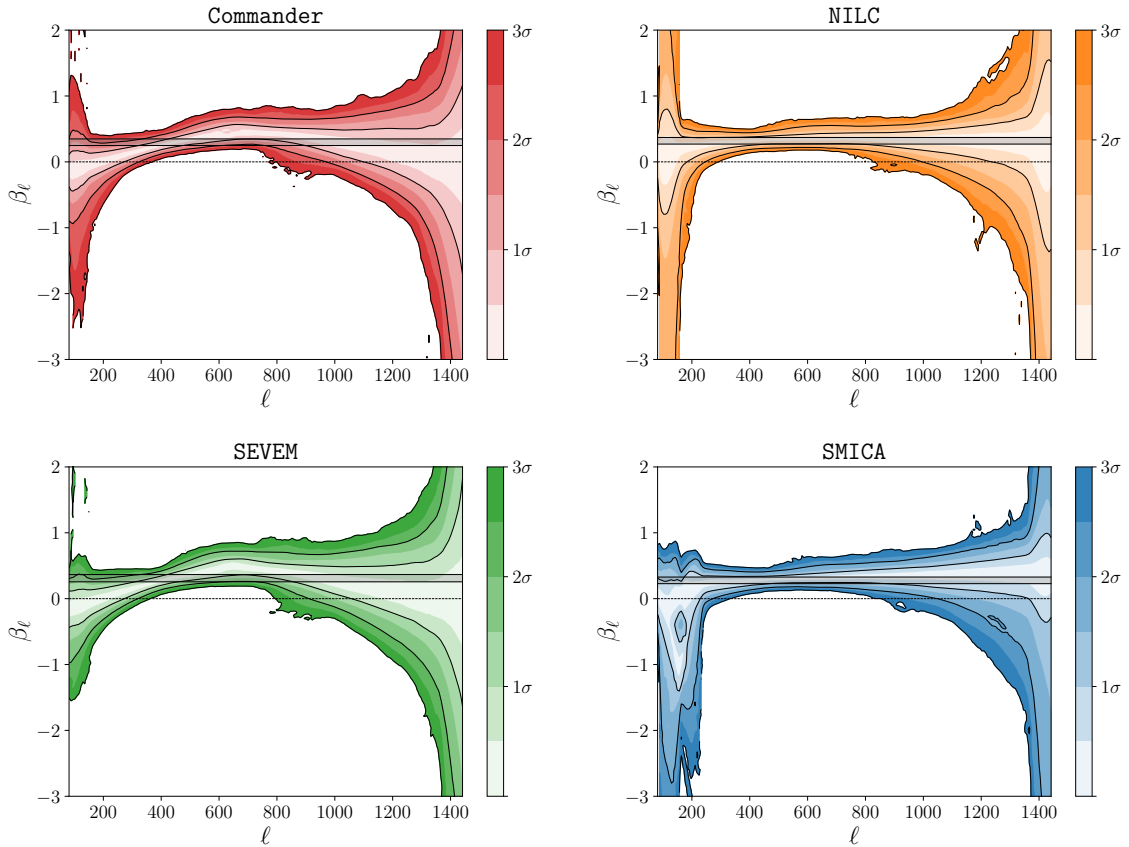


**Figure 7:** Reconstruction of the angular isotropic cosmic birefringence angle plotted using iso-probability credibility intervals in the  $(\beta_\ell, \ell)$  plane, with their masses converted to  $\sigma$  values via an inverse error function transformation, obtained from the  $EB$ -based estimator applied to the *Commander*, *NILC*, *SEVEM*, and *SMICA* maps, assuming four nodes ( $N = 4$ ). The grey band correspond to the result obtained with  $N = 1$  collected on table 3. The grey shadow regions correspond to the 68% CL obtained performing the same analysis with one node ( $N = 1$ ).

Method	$\beta$ [deg]
PR3 <i>Commander</i>	$0.30 \pm 0.05$
PR3 <i>NILC</i>	$0.32 \pm 0.05$
PR3 <i>SEVEM</i>	$0.31 \pm 0.06$
PR3 <i>SMICA</i>	$0.28 \pm 0.05$

**Table 3:** Mean values of  $\beta$  and uncertainties at 68% CL obtained with PolyChord considering one node ( $N = 1$ ).

In appendix B, we collect the results obtained from this pipeline varying the number of nodes compared to the results showed here for  $N = 4$  as well as the Bayes factor calculated with respect to the case with one node.

Parameter	LiteBIRD	SO-LAT	CMB-S4
beam [arcmin]	30	1.4	1
sensitivity [ $\mu K \cdot \text{arcmin}$ ]	3.26	8.49	4.24
sky fraction	70%	40%	2%
$N_{\text{side}}$	1024	1024	2048
$\ell_{\text{min}}$	11	11	51
$\ell_{\text{max}}$	811	3011	3011

**Table 4:** Summary of the experimental specifications for the considered upcoming CMB surveys (upper block), and the set-up for the analysis pipeline (lower block).

## 4 Forecasts for future CMB experiments

In this section, we present forecasts on our ability to recover  $\beta_0$  and  $n$  using upcoming CMB experiments. In particular, we focus on the following experiments: LiteBIRD (LB) [63, 64], Simons Observatory - Large Aperture Telescope (SO-LAT) [65, 66], and CMB Stage 4 (CMB-S4) [67, 68].

For each experiment, we produce 500 simulated datasets, with the same underlying cosmological parameters, including a scale-invariant angle  $\beta$  of 0.3 deg, but with different noise phases with the experimental configurations as reported in the upper block of table 4. We then apply the analysis pipeline presented in section 3.3 to constrain  $\beta_0$  and  $n$ . We use the same pivot scale as in the *Planck* analysis to make the estimate of  $n$  from the forecasts to be comparable with the one from the analysis in this work.<sup>15</sup> The forecasts for  $\beta_0$  and  $n$  are presented in table 5. The uncertainty on  $\beta_0$  is up to 5 times lower than that obtained with *Planck* data, and the error on  $n$  can be up to  $\sim 7$  times lower than the larger error found with *Planck* data.

Par.	LiteBIRD	SO-LAT	CMB-S4
$\beta_0$ [deg]	$0.30 \pm 0.01$	$0.30 \pm 0.01$	$0.30 \pm 0.02$
$n$	$0.00 \pm 0.07$	$0.00 \pm 0.05$	$0.00 \pm 0.07$

**Table 5:** Forecasted best-fit values and  $1\sigma$  errors for  $(\beta_0, n)$  from upcoming CMB experiments.

## 5 Conclusions

In this work, we use the *Planck* PR3 data and simulations to constrain the dependence of the cosmic birefringence angle  $\beta$  on the harmonic scale  $\ell$ . Such a dependence might stem from ChS models if the mass of the pseudo-scalar field is not sufficiently small. In this case, the main observational signature is represented by the  $EB$  spectrum that is not a perfect rescaling of  $(EE - BB)/2$ , a condition that would break the degeneracy between the CB isotropic angle and the instrumental polarisation angle.

Using the data and simulations as described in section 2, we confirm the presence of an excess of  $EB$  signal across all four CS methods, whose origin remains unclear. We find

<sup>15</sup>This choice does not necessarily represent the optimal choice for different experimental set-ups.

that the estimated  $\beta$  over the whole harmonic range, i.e.  $[42,1501]$ , is consistent with the literature [18, 19] regardless of the impact of the instrumental polarisation angle.

We have studied the harmonic dependence of this excess, through two different methods: a parametric approach, where we fit the data using the power law in eq. (3.7), and a non-parametric approach based on the `FlexKnot` model. The excess is found to be independent from the harmonic scale, at the  $\lesssim 2\sigma$  level, for all CS methods. Using the non-parametric approach with the `FlexKnot` model we find a strong preference for a constant  $\beta$  angle across the harmonic range (see fig. 10).

The main outcome of this work ultimately lies in the *Planck* data preference for a constant value of the CB angle across the harmonic scales [26, 32, 33]. Future CMB experiments will further reduce *Planck* uncertainties up to a factor of 7. If the effect is due to new physics, these findings would provide strong constraints on the ultra-light nature of the axion field with even better perspectives for future probes.

## A Pivot scale

We assess the choice of the pivot scale  $\ell_{B_0}$  by examining three different choices for  $B_0$  across the four CS *Planck* datasets. We select the bin that results in the smallest correlation between  $\beta_0$  and  $n$  while being compatible with the value of  $\beta$  estimated across the entire range and yielding the smallest possible systematic uncertainty on  $n$  from  $\beta_{\text{res}}$ . Tables 6 and 7 report our numerical results for the four CS datasets and for three choices of  $B_0$  corresponding to the third ( $\ell \in [202, 281]$ ), sixth ( $\ell \in [442, 521]$ ) and tenth ( $\ell \in [762, 841]$ ) bins. We also show in fig. 8 the corresponding contour plots. We find that a common value of  $B_0 = 6$  minimises both the correlation between the model parameters and the systematic uncertainty for  $n$ . This position corresponds to the region most constrained by the non-parametric reconstruction; see fig. 7.

Par.	Pivot scale	Data considered: $\beta_B$			
		Commander	NILC	SEVEM	SMICA
$\beta_0$ [deg]	3rd bin	$0.19^{+0.07}_{-0.06}$	$0.26 \pm 0.07$	$0.20^{+0.07}_{-0.06}$	$0.19^{+0.07}_{-0.06}$
	6th bin	$0.28 \pm 0.05$	$0.31 \pm 0.05$	$0.30 \pm 0.06$	$0.26 \pm 0.05$
	10th bin	$0.39 \pm 0.07$	$0.36 \pm 0.07$	$0.41 \pm 0.08$	$0.36 \pm 0.07$
$n$	3rd bin	$0.53^{+0.33}_{-0.31}$	$0.23^{+0.30}_{-0.29}$	$0.51^{+0.32}_{-0.30}$	$0.44^{+0.35}_{-0.33}$
	6th bin	$0.60^{+0.34}_{-0.31}$	$0.29^{+0.31}_{-0.29}$	$0.57^{+0.33}_{-0.31}$	$0.52^{+0.36}_{-0.34}$
	10th bin	$0.65^{+0.35}_{-0.32}$	$0.34^{+0.32}_{-0.30}$	$0.62^{+0.34}_{-0.31}$	$0.58^{+0.37}_{-0.34}$

**Table 6:** Best-fit values and  $1\sigma$  errors for  $(\beta_0, n)$  at different pivot scales (3rd, 6th, and 10th bin corresponding respectively to  $\ell_{B_0} = 242, 482, 802$ ) for the various CS methods.

## B Non-parametric Bayesian reconstruction for $N \neq 4$ nodes

Figure 9 shows the evolution of the reconstructed function as the number of nodes changes with respect to the case considered in section 3.4 for  $N = 4$ , with the shaded regions representing the credible intervals derived from the posterior samples. The results show how

Par.	Pivot scale	Data considered: $\beta_{\text{res}}$			
		Commander	NILC	SEVEM	SMICA
$\beta_0$ [deg]	3rd bin	$0.019 \pm 0.005$	$0.014 \pm 0.005$	$0.014 \pm 0.005$	$0.017 \pm 0.005$
	6th bin	$0.019 \pm 0.003$	$0.013 \pm 0.003$	$0.013 \pm 0.003$	$0.017 \pm 0.003$
	10th bin	$0.019 \pm 0.004$	$0.014 \pm 0.004$	$0.014^{+0.005}_{-0.004}$	$0.017 \pm 0.004$
$n$	3rd bin	$-0.07^{+0.33}_{-0.29}$	$-0.12^{+0.42}_{-0.38}$	$-0.12^{+0.45}_{-0.38}$	$-0.08^{+0.36}_{-0.31}$
	<b>6th bin</b>	<b><math>0.00^{+0.35}_{-0.31}</math></b>	<b><math>0.00^{+0.45}_{-0.41}</math></b>	<b><math>0.00^{+0.49}_{-0.41}</math></b>	<b><math>0.00^{+0.38}_{-0.33}</math></b>
	10th bin	$0.05^{+0.36}_{-0.32}$	$0.09^{+0.47}_{-0.42}$	$0.10^{+0.53}_{-0.44}$	$0.06^{+0.39}_{-0.34}$

**Table 7:** Best-fit values and  $1\sigma$  errors for  $(\beta_0, n)$  at different pivot scales (3rd, 6th, and 10th bin), estimated from the bias term  $\beta_{\text{res}}$  for various CS methods. We highlighted with bold text the sixth bin row corresponding to the minimal value recovered for  $n$ .

increasing the number of nodes improves the ability of the reconstruction to capture fine features of the data, while also highlighting the diminishing returns as the number of nodes becomes excessive, leading to potential overfitting. This is also described by the worsening of the Bayes factor as the number of nodes increases; see fig. 10. The result agrees well with the best fit obtained with the power-law template showed in table 2 and fig. 5.

## Acknowledgments

We thank Patricia Diego-Palazuelos for her valuable feedback on the draft version of the manuscript. We acknowledge financial support from the INFN InDark initiative and from the COSMOS network through the ASI (Italian Space Agency) Grants 2016-24-H.0, 2016-24-H.1-2018, 2020-9-HH.0 (participation in LiteBIRD phase A). SSS acknowledges that this publication was produced while attending the PhD program in Space Science and Technology at the University of Trento, Cycle XXXVIII, with the support of a scholarship co-financed by the Ministerial Decree no. 351 of 9th April 2022, based on the NRRP - funded by the European Union - NextGenerationEU - Mission 4 "Education and Research", Component 2 "From Research to Business", Investment 3.3. SSS acknowledges that this publication is based upon work from COST Action CA21136 – "Addressing observational tensions in cosmology with systematics and fundamental physics (CosmoVerse)", supported by COST (European Cooperation in Science and Technology). AG, PN and SP acknowledge support by the MUR PRIN2022 Project "BROWSEPOL: Beyond standaRd mOdel With coSmic microwavE background POLarization"-2022EJNZ53 financed by the European Union - Next Generation EU.

**Note added.** While we were completing our manuscript, we learned of the decision by DOE and NSF to no longer support the CMB-S4 Project. Nevertheless, we decided to keep our CMB-S4 forecast in our analysis.

## References

- [1] S.M. Carroll, G.B. Field and R. Jackiw, *Limits on a Lorentz and Parity Violating Modification of Electrodynamics*, *Phys. Rev. D* **41** (1990) 1231.

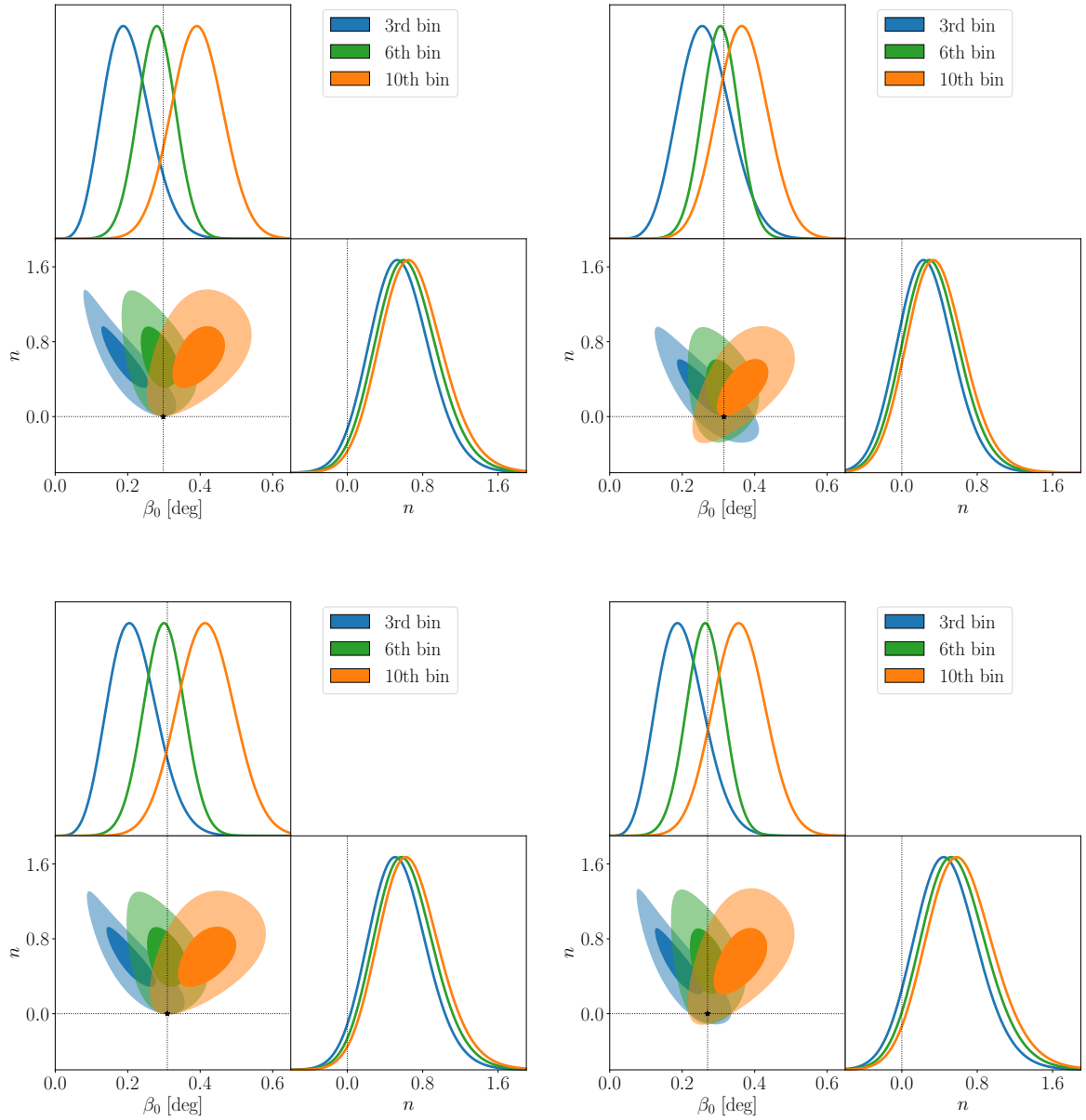


**Figure 8:** Triangular plots reporting the power-law test results for all four CS methods: Commander (top left), NILC (top right), NILC (bottom left) and SMICA (bottom right), using  $D^{EB}$  estimator and varying the pivotal bin (3rd, 6th or 10th).

- [2] S.M. Carroll and G.B. Field, *The Einstein equivalence principle and the polarization of radio galaxies*, *Phys. Rev. D* **43** (1991) 3789.
- [3] D. Harari and P. Sikivie, *Effects of a Nambu-Goldstone boson on the polarization of radio galaxies and the cosmic microwave background*, *Phys. Lett. B* **289** (1992) 67.
- [4] S.M. Carroll, *Quintessence and the rest of the world*, *Phys. Rev. Lett.* **81** (1998) 3067 [[astro-ph/9806099](#)].
- [5] W.-T. Ni, *Equivalence Principles and Electromagnetism*, *Phys. Rev. Lett.* **38** (1977) 301.

- [6] W.-T. Ni, *A nonmetric theory of gravity*, *Int. J. Mod. Phys. D* **25** (2016) 1640017.
- [7] E. Komatsu, *New physics from the polarized light of the cosmic microwave background*, *Nature Rev. Phys.* **4** (2022) 452 [2202.13919].
- [8] A. Lue, L.-M. Wang and M. Kamionkowski, *Cosmological signature of new parity violating interactions*, *Phys. Rev. Lett.* **83** (1999) 1506 [astro-ph/9812088].
- [9] B. Feng, H. Li, M.-z. Li and X.-m. Zhang, *Gravitational leptogenesis and its signatures in CMB*, *Phys. Lett. B* **620** (2005) 27 [hep-ph/0406269].
- [10] G.-C. Liu, S. Lee and K.-W. Ng, *Effect on cosmic microwave background polarization of coupling of quintessence to pseudoscalar formed from the electromagnetic field and its dual*, *Phys. Rev. Lett.* **97** (2006) 161303 [astro-ph/0606248].
- [11] F. Finelli and M. Galaverni, *Rotation of Linear Polarization Plane and Circular Polarization from Cosmological Pseudo-Scalar Fields*, *Phys. Rev. D* **79** (2009) 063002 [0802.4210].
- [12] M.A. Fedderke, P.W. Graham and S. Rajendran, *Axion Dark Matter Detection with CMB Polarization*, *Phys. Rev. D* **100** (2019) 015040 [1903.02666].
- [13] M. Galaverni, F. Finelli and D. Paoletti, *Redshift evolution of cosmic birefringence in CMB anisotropies*, *Phys. Rev. D* **107** (2023) 083529 [2301.07971].
- [14] PLANCK collaboration, *Planck intermediate results. XLIX. Parity-violation constraints from polarization data*, *Astron. Astrophys.* **596** (2016) A110 [1605.08633].
- [15] B.G. Keating, M. Shimon and A.P.S. Yadav, *Self-Calibration of CMB Polarization Experiments*, *Astrophys. J. Lett.* **762** (2012) L23 [1211.5734].
- [16] Y. Minami, H. Ochi, K. Ichiki, N. Katayama, E. Komatsu and T. Matsumura, *Simultaneous determination of the cosmic birefringence and miscalibrated polarization angles from CMB experiments*, *PTEP* **2019** (2019) 083E02 [1904.12440].
- [17] Y. Minami and E. Komatsu, *Simultaneous determination of the cosmic birefringence and miscalibrated polarization angles II: Including cross frequency spectra*, *PTEP* **2020** (2020) 103E02 [2006.15982].
- [18] Y. Minami and E. Komatsu, *New Extraction of the Cosmic Birefringence from the Planck 2018 Polarization Data*, *Phys. Rev. Lett.* **125** (2020) 221301 [2011.11254].
- [19] P. Diego-Palazuelos et al., *Cosmic Birefringence from the Planck Data Release 4*, *Phys. Rev. Lett.* **128** (2022) 091302 [2201.07682].
- [20] P. Diego-Palazuelos, E. Martínez-González, P. Vielva, R. Barreiro, M. Tristram, E. de la Hoz et al., *Robustness of cosmic birefringence measurement against galactic foreground emission and instrumental systematics*, *Journal of Cosmology and Astroparticle Physics* **2023** (2023) 044.
- [21] J.R. Eskilt and E. Komatsu, *Improved constraints on cosmic birefringence from the WMAP and Planck cosmic microwave background polarization data*, *Phys. Rev. D* **106** (2022) 063503 [2205.13962].
- [22] A. Gruppuso and S. di Serego Alighieri, *Cosmic Polarisation Rotation from CMB Data: a Review for GR110*, 2502.07743.
- [23] ACT collaboration, *The Atacama Cosmology Telescope: DR6 Power Spectra, Likelihoods and  $\Lambda$ CDM Parameters*, 2503.14452.
- [24] R.M. Sullivan, A. Abghari, P. Diego-Palazuelos, L.T. Hergt and D. Scott, *Planck PR4 (NPIPE) map-space cosmic birefringence*, 2502.07654.
- [25] COMPACT collaboration, *Cosmic topology. Part IIIa. Microwave background parity violation without parity-violating microphysics*, *JCAP* **11** (2024) 020 [2407.09400].

- [26] H. Nakatsuka, T. Namikawa and E. Komatsu, *Is cosmic birefringence due to dark energy or dark matter? A tomographic approach*, *Phys. Rev. D* **105** (2022) 123509 [2203.08560].
- [27] A. Greco, N. Bartolo and A. Gruppuso, *A new solution for the observed isotropic cosmic birefringence angle and its implications for the anisotropic counterpart through a Boltzmann approach*, *JCAP* **10** (2024) 028 [2401.07079].
- [28] T. Fujita, K. Murai, H. Nakatsuka and S. Tsujikawa, *Detection of isotropic cosmic birefringence and its implications for axionlike particles including dark energy*, *Phys. Rev. D* **103** (2021) 043509 [2011.11894].
- [29] L. Yin, J. Kochappan, T. Ghosh and B.-H. Lee, *Is cosmic birefringence model-dependent?*, *JCAP* **10** (2023) 007 [2305.07937].
- [30] J. Kochappan, L. Yin, B.-H. Lee and T. Ghosh, *Observational evidence for Early Dark Energy as a unified explanation for Cosmic Birefringence and the Hubble tension*, 2408.09521.
- [31] A. Greco, N. Bartolo and A. Gruppuso, *Probing Axions through Tomography of Anisotropic Cosmic Birefringence*, *JCAP* **05** (2023) 026 [2211.06380].
- [32] J.R. Eskilt, L. Herold, E. Komatsu, K. Murai, T. Namikawa and F. Naokawa, *Constraints on Early Dark Energy from Isotropic Cosmic Birefringence*, *Phys. Rev. Lett.* **131** (2023) 121001 [2303.15369].
- [33] T. Namikawa, K. Murai and F. Naokawa, *Planck Constraints on Axion-Like Particles through Isotropic Cosmic Birefringence*, 2506.20824.
- [34] PLANCK collaboration, *Planck 2018 results. I. Overview and the cosmological legacy of Planck*, *Astron. Astrophys.* **641** (2020) A1 [1807.06205].
- [35] W.J. Handley, M.P. Hobson and A.N. Lasenby, *PolyChord: nested sampling for cosmology*, *Mon. Not. Roy. Astron. Soc.* **450** (2015) L61 [1502.01856].
- [36] W.J. Handley, M.P. Hobson and A.N. Lasenby, *polychord: next-generation nested sampling*, *Mon. Not. Roy. Astron. Soc.* **453** (2015) 4385 [1506.00171].
- [37] A. Raffaelli and M. Ballardini, *Knot reconstruction of the scalar primordial power spectrum with Planck, ACT, and SPT CMB data*, *arXiv e-prints* (2025) arXiv:2503.10609 [2503.10609].
- [38] H.K. Eriksen et al., *CMB component separation by parameter estimation*, *Astrophys. J.* **641** (2006) 665 [astro-ph/0508268].
- [39] H.K. Eriksen, J.B. Jewell, C. Dickinson, A.J. Banday, K.M. Gorski and C.R. Lawrence, *Joint Bayesian component separation and CMB power spectrum estimation*, *Astrophys. J.* **676** (2008) 10 [0709.1058].
- [40] J. Delabrouille, J.F. Cardoso, M.L. Jeune, M. Betoule, G. Fay and F. Guilloux, *A full sky, low foreground, high resolution CMB map from WMAP*, *Astron. Astrophys.* **493** (2009) 835 [0807.0773].
- [41] E. Martinez-Gonzalez, J.M. Diego, P. Vielva and J. Silk, *CMB power spectrum estimation and map reconstruction with the expectation - Maximization algorithm*, *Mon. Not. Roy. Astron. Soc.* **345** (2003) 1101 [astro-ph/0302094].
- [42] J. Delabrouille, J.F. Cardoso and G. Patanchon, *Multi-detector multi-component spectral matching and applications for CMB data analysis*, *Mon. Not. Roy. Astron. Soc.* **346** (2003) 1089 [astro-ph/0211504].
- [43] J.-F. Cardoso, M. Martin, J. Delabrouille, M. Betoule and G. Patanchon, *Component separation with flexible models. Application to the separation of astrophysical emissions*, 0803.1814.
- [44] S.M. Leach et al., *Component separation methods for the Planck mission*, *Astron. Astrophys.* **491** (2008) 597 [0805.0269].

- [45] PLANCK collaboration, *Planck 2018 results. IV. Diffuse component separation*, *Astron. Astrophys.* **641** (2020) A4 [[1807.06208](#)].
- [46] M. Bortolami, M. Billi, A. Gruppuso, P. Natoli and L. Pagano, *Planck constraints on cross-correlations between anisotropic cosmic birefringence and CMB polarization*, *JCAP* **09** (2022) 075 [[2206.01635](#)].
- [47] J.A. Tauber, N. Mandolesi, J.L. Puget, T. Banos, M. Bersanelli, F.R. Bouchet et al., *Planck pre-launch status: The Planck mission*, *AA* **520** (2010) A1.
- [48] PLANCK collaboration, *Planck 2015 results. XII. Full Focal Plane simulations*, *Astron. Astrophys.* **594** (2016) A12 [[1509.06348](#)].
- [49] PLANCK collaboration, *Planck 2018 results. III. High Frequency Instrument data processing and frequency maps*, *Astron. Astrophys.* **641** (2020) A3 [[1807.06207](#)].
- [50] K.M. Górski, E. Hivon, A.J. Banday, B.D. Wandelt, F.K. Hansen, M. Reinecke et al., *HEALPix - A Framework for high resolution discretization, and fast analysis of data distributed on the sphere*, *Astrophys. J.* **622** (2005) 759 [[astro-ph/0409513](#)].
- [51] LSST DARK ENERGY SCIENCE collaboration, *A unified pseudo- $C_\ell$  framework*, *Mon. Not. Roy. Astron. Soc.* **484** (2019) 4127 [[1809.09603](#)].
- [52] E. Hivon, K.M. Gorski, C.B. Netterfield, B.P. Crill, S. Prunet and F. Hansen, *Master of the cosmic microwave background anisotropy power spectrum: a fast method for statistical analysis of large and complex cosmic microwave background data sets*, *Astrophys. J.* **567** (2002) 2 [[astro-ph/0105302](#)].
- [53] G. Polenta, D. Marinucci, A. Balbi, P. de Bernardis, E. Hivon, S. Masi et al., *Unbiased estimation of angular power spectrum*, *JCAP* **11** (2005) 001 [[astro-ph/0402428](#)].
- [54] A. Lewis, A. Challinor and N. Turok, *Analysis of CMB polarization on an incomplete sky*, *Phys. Rev. D* **65** (2002) 023505 [[astro-ph/0106536](#)].
- [55] E.F. Bunn, M. Zaldarriaga, M. Tegmark and A. de Oliveira-Costa, *E/B decomposition of finite pixelized CMB maps*, *Phys. Rev. D* **67** (2003) 023501 [[astro-ph/0207338](#)].
- [56] J. Grain, M. Tristram and R. Stompor, *Polarized CMB spectrum estimation using the pure pseudo cross-spectrum approach*, *Phys. Rev. D* **79** (2009) 123515 [[0903.2350](#)].
- [57] QUAD collaboration, *Parity Violation Constraints Using Cosmic Microwave Background Polarization Spectra from 2006 and 2007 Observations by the QUaD Polarimeter*, *Phys. Rev. Lett.* **102** (2009) 161302 [[0811.0618](#)].
- [58] A. Gruppuso, G. Maggio, D. Molinari and P. Natoli, *A note on the birefringence angle estimation in CMB data analysis*, *JCAP* **05** (2016) 020 [[1604.05202](#)].
- [59] J. Hartlap, P. Simon and P. Schneider, *Why your model parameter confidences might be too optimistic: Unbiased estimation of the inverse covariance matrix*, *Astron. Astrophys.* **464** (2007) 399 [[astro-ph/0608064](#)].
- [60] M. Millea and F. Bouchet, *Cosmic Microwave Background Constraints in Light of Priors Over Reionization Histories*, *Astron. Astrophys.* **617** (2018) A96 [[1804.08476](#)].
- [61] W.J. Handley, A.N. Lasenby, H.V. Peiris and M.P. Hobson, *Bayesian inflationary reconstructions from Planck 2018 data*, *Phys. Rev. D* **100** (2019) 103511 [[1908.00906](#)].
- [62] W. Handley, *fgivenx: Functional posterior plotter*, *The Journal of Open Source Software* **3** (2018) .
- [63] LiteBIRD Collaboration, E. Allys, K. Arnold, J. Aumont, R. Aurlien, S. Azzoni et al., *Probing cosmic inflation with the litebird cosmic microwave background polarization survey*, *Progress of Theoretical and Experimental Physics* **2023** (2022) 042F01 [<https://academic.oup.com/ptep/article-pdf/2023/4/042F01/50954267/ptac150.pdf>].

- [64] E. de la Hoz et al., *LiteBIRD Science Goals and Forecasts: constraining isotropic cosmic birefringence*, [2503.22322](#).
- [65] P. Ade, J. Aguirre, Z. Ahmed, S. Aiola, A. Ali, D. Alonso et al., *The simons observatory: science goals and forecasts*, *Journal of Cosmology and Astroparticle Physics* **2019** (2019) 056.
- [66] SIMONS OBSERVATORY collaboration, *The Simons Observatory: Science Goals and Forecasts for the Enhanced Large Aperture Telescope*, [2503.00636](#).
- [67] K. Abazajian, G.E. Addison, P. Adshead, Z. Ahmed, D. Akerib, A. Ali et al., *Cmb-s4: Forecasting constraints on primordial gravitational waves*, *The Astrophysical Journal* **926** (2022) 54.
- [68] E. Schiappucci, S. Raghunathan, C. To, F. Bianchini, C.L. Reichardt, N. Battaglia et al., *Constraining cosmological parameters using the pairwise kinematic sunyaev-zel'dovich effect with cmb-s4 and future galaxy cluster surveys*, 2024.

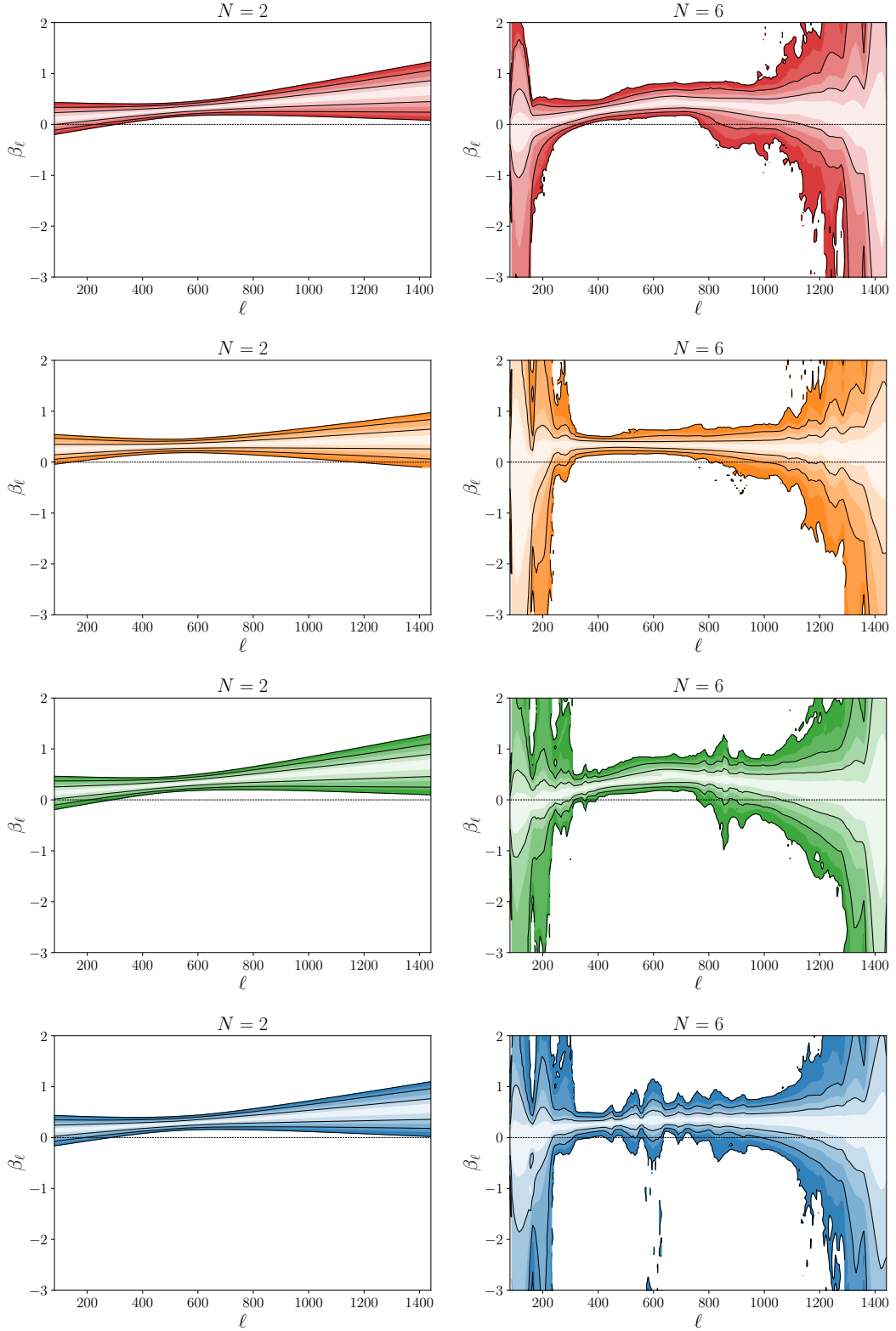


**Figure 9:** Reconstruction of the angular isotropic cosmic birefringence angle plotted using iso-probability credibility intervals in the  $(\beta_\ell, \ell)$  plane, with their masses converted to  $\sigma$ -values via an inverse error function transformation, obtained from the  $EB$ -based estimator applied to (from top to bottom) the Commander, NILC, SEVEM and SMICA maps for  $N = 2$  (left panels) and  $N = 6$  (right panels).

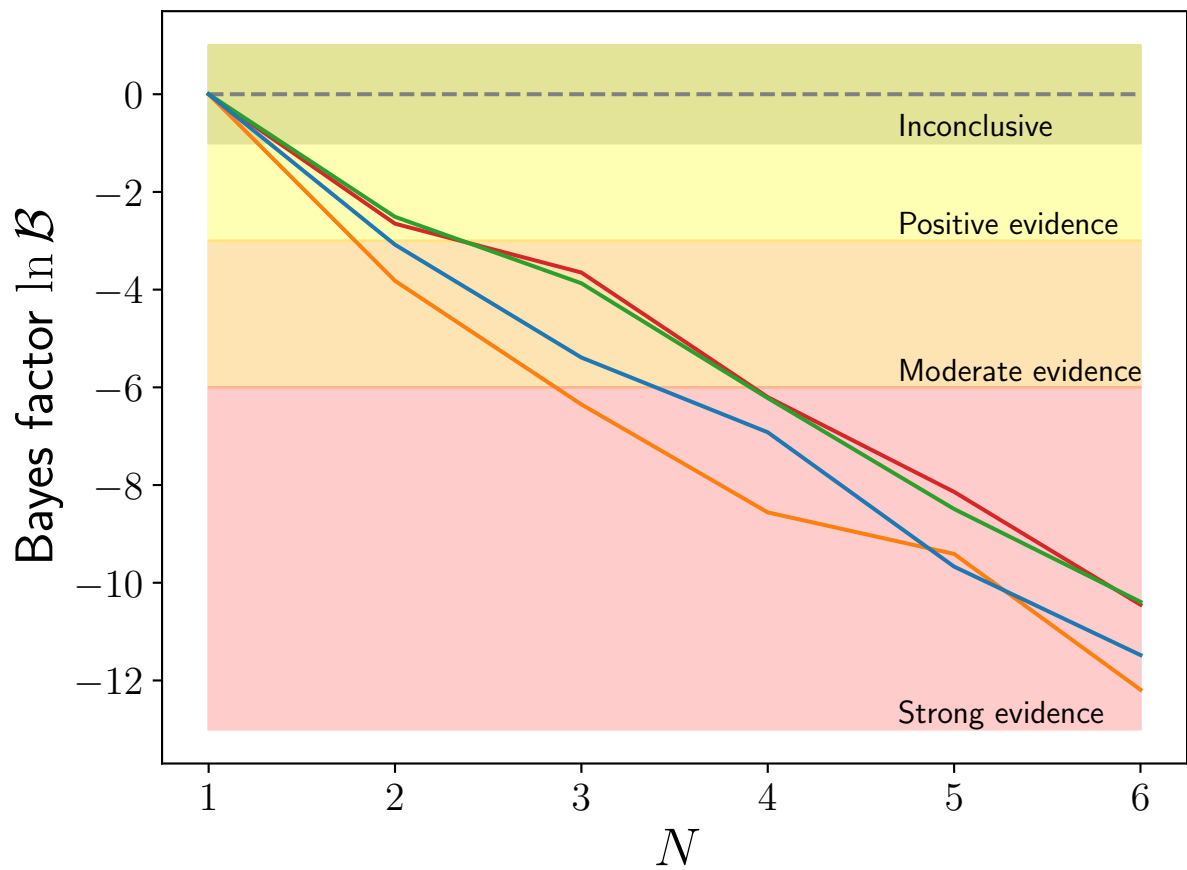


**Figure 10:** Bayesian evidence as a function of number of nodes  $N$  for the isotropic cosmic birefringence angle reconstruction.